

---

# Plasma diagnostics of supernova remnant 3C 400.2 by Suzaku observations

Masataka ONUMA<sup>1,\*</sup>, Kumiko K. NOBUKAWA<sup>1,\*</sup>, Masayoshi NOBUKAWA<sup>2</sup>,  
Shigeo YAMAUCHI<sup>3</sup>, Hideki UCHIYAMA<sup>4</sup>,

<sup>1</sup>Faculty of Science and Engineering, Kindai University, 3-4-1 Kowakae, Higashi-Osaka,  
577-8502, Japan

<sup>2</sup>Department of Teacher Training and School Education, Nara University of Education,  
Takabatake-cho, Nara, 630-8528, Japan

<sup>3</sup>Faculty of Science, Nara Women's University, Kitauoyanishi-machi, Nara, Nara 630-8506,  
Japan

<sup>4</sup>Faculty of Education, Shizuoka University, 836 Ohya, Suruga-ku, Shizuoka, Shizuoka,  
422-8529, Japan

\*E-mail: kumiko@phys.kindai.ac.jp

Received (reception date); Accepted (acceptation date)

## Abstract

We report a result of plasma diagnostics of the supernova remnant (SNR) 3C 400.2, which has been reported to have a recombining plasma (RP) by previous studies. For careful background estimation, we simultaneously fitted spectra extracted from the SNR and background regions and evaluated the SNR emission contaminating the background-region spectrum as well as the background emission in the source-region spectrum. The SNR emission is explained by the collisional ionization equilibrium plasma originating from the interstellar medium and the ionizing plasma originating from the ejecta, in contrast to the previous studies. In addition, we found an unidentified X-ray source near the SNR, Suzaku J1937.4+1718, which is accompanied by an emission line at  $\sim 4.4$  keV with the  $2.8\sigma$  confidence level. Since there is no striking atomic line at the energy in the rest frame, Suzaku J1937.4+1718 can be an extragalactic object with a redshifted Fe line.

**Key words:** ISM: individual objects (3C 400.2) — ISM: supernova remnants — X-rays: ISM

---

## 1 Introduction

3C 400.2 is a Galactic supernova remnant (SNR) located at a distance of  $2.8 \pm 0.8$  kpc (Giacani et al. 1998) and its age is estimated to be  $10^4$ – $10^5$  years old (Long et al. 1991; Rosado 1983). Its radio morphology shows two overlapping circular shells with diameters of 14' and 22' (Dubner et al. 1994). Its optical appearance is shell-like with a radius of approximately 8' (Winkler et al. 1993; Ambrocio-Cruz et al. 2006). Giacani et al. (1998) reported that dense H I gas overlaps with the radio shell in the northwest of the SNR. Ergin et al. (2017) found an expanding shell in the position-velocity diagram of H I, the di-

ameter of which is similar to that of the SNR. This indicates the interaction between the H I cloud and the SNR shell. Although there is no dense atomic and molecular gas inside the shell, GeV gamma-ray emission was found from the inside (Ergin et al. 2017), and the mechanism of the gamma-ray emission is debatable. The Einstein Image Proportional Counter (IPC) and the ROSAT Position Sensitive Proportional Counter (PSPC) revealed an X-ray peak at the center of 3C 400.2, which was correlated with neither the radio features nor the optical filaments (Long et al. 1991; Saken et al. 1995), and thus 3C 400.2 was classified into mixed-morphology SNRs (Rho & Petre 1998). The X-ray spectrum obtained by ASCA was well explained by

a thin thermal plasma in collisional ionization equilibrium (CIE) with the temperature of  $kT_e=0.5\text{--}0.8$  keV (Yoshita et al. 2001).

A recombining plasma (RP) of 3C 400.2 was reported by most recent X-ray studies conducted by Chandra and Suzaku. Broersen et al. (2015) analyzed the Chandra data and claimed that the X-ray spectrum could be explained by two components: an RP originated from the interstellar medium (ISM) ( $kT_e \sim 0.1$  keV) and an ionizing plasma (IP) originated from the ejecta ( $kT_e \sim 3$  keV). Ergin et al. (2017), on the other hand, obtained a result inconsistent with the Chandra result using the Suzaku data; the X-ray spectrum of the eastern region was explained by a CIE plasma originated from the ISM ( $kT_e = 0.3\text{--}0.5$  keV) and an RP originated from the ejecta ( $kT_e = 0.6\text{--}0.7$  keV) whereas that of the western region was explained by a CIE plasma of the ISM ( $kT_e = 0.3\text{--}0.4$  keV) plus an IP of the ejecta ( $kT_e = 0.7$  keV). This discrepancy between the Chandra and Suzaku results may be due to the differences in the way to estimate the background. Broersen et al. (2015) used the standard ACIS-I background files to produce the background spectra, whereas Ergin et al. (2017) estimated the background spectra by extracting the data from nearby regions of the same observations as the SNR.

In this paper, we reanalyzed the Suzaku data of 3C 400.2 with a careful estimation of the background emission to diagnose the plasma state. We performed a simultaneous fitting of spectra extracted from a source region and nearby background region to take into account the SNR emission contaminating the background-region spectrum. We also report a discovery of an unidentified X-ray source near 3C 400.2 and its spectral analysis result. The errors in the figures are shown in the  $1\sigma$  level, and the uncertainties are quoted at the 90% confidence range unless otherwise stated.

## 2 Observations and Data Reduction

Suzaku (Mitsuda et al. 2007) observed four regions of 3C 400.2 with the X-ray imaging spectrometer (XIS; Koyama et al. 2007), covering the whole SNR. The XIS is placed on the focal plane of the X-Ray Telescope (XRT; Serlemitsos et al. 2007). The field of view (FOV) of the XIS is  $17'.8 \times 17'.8$ . The XIS consists of four X-ray charge-coupled devices (CCDs). XIS1 is a backside illuminated (BI) device, while XIS0, 2, and 3 are frontside illuminated (FI) devices. XIS2 has been dysfunctional since November 9, 2006. A small fraction of XIS0 has been non-functional since June 23, 2009, due to a micro-meteorite impact. We therefore used the data obtained by the remaining parts of XIS0, XIS1, and XIS3. We downloaded the Suzaku archival data of 3C 400.2 as well as EMS 1308 for the background estimation via the Data Archives and Transmission System (DARTS; <https://www.darts.isas.jaxa.jp/index.html.en>). The observation log is shown in

table 1.

For extracting images and spectra, we used HEASoft version 6.31 and the calibration database version 2018-06-11. The spectral analysis was carried out with XSPEC version 12.10.0. The effective area of the XRT (ancillary response files; ARF) and the response of the XIS (redistribution matrix files; RMF) were calculated using `xissimarfgen` (Ishisaki et al. 2007) and `xisrmfgen`, respectively. The non X-ray background (NXB) was estimated using `xisnxbgen` (Tawa et al. 2008).

## 3 Analysis and Results

### 3.1 X-ray Images

Figure 1 shows X-ray images of 3C 400.2 in the 0.5–3.0 keV and 3.0–5.0 keV energy bands. The NXB was subtracted, and the vignetting effect was corrected. The images of XIS0, 1, and 3 were all merged. We see a diffuse emission due to the SNR in the low energy band, while little X-ray emission other than a point-like source in the high energy band. The coordinate of the point-like source was  $(\alpha, \delta)_{J2000} = (19^h 37^m 36.^s 13, 17^\circ 18' 53.'' 82)$  with a positional uncertainty of  $19''$  (Uchiyama et al. 2008). It has not been reported in any catalog so far. Then we named this object Suzaku J1937.4+1718.

### 3.2 Background estimation

We extracted spectra from the whole SNR region and the background region (hereafter, the BGD region), respectively. The former region is enclosed by a solid polygon, and the latter region is surrounded by the dashed lines in figure 1(a). The FI (XIS0 and 3) spectra were merged, and the FI and BI spectra were simultaneously fitted.

The X-ray emission of the SNR covers most of the FOV of the four 3C400.2 pointings and it can contaminate the BGD-region spectrum due to the outer skirt of the point spread function (PSF) of the XRT. Subtracting the contaminated BGD spectrum from the SNR spectrum results in underestimating the SNR emission flux, and also can affect the best-fit parameters. Hence, we conducted simultaneous fitting of the whole SNR and BGD spectra and evaluated the SNR and the background emission fluxes in each region. Simultaneous fitting of source and background spectra has been conducted by several previous studies (Konami et al. 2012, Ono et al. 2019, Yamauchi et al. 2023).

We generated two ARFs for the whole SNR spectrum: one is for the SNR emission (as an extended source) observed in the whole region, and the other is for the background emission (as a uniform sky) observed in the whole region. Applying the two different ARFs to the two models follows the XSPEC manual described in <https://heasarc.gsfc.nasa.gov/xanadu/xspec/manual/node40.html>. Similarly,

**Table 1.** Observation log.

region name	Obs ID	pointing direction		observation time		exposure time (ks)
		$l(^{\circ})$	$b(^{\circ})$	Start (UT)	End(UT)	
3C400.2 NW	509068010	53 $^{\circ}$ .68	-2 $^{\circ}$ .00	2014/4/23 11:08:52	2014/4/23 22:35:09	21.5
3C400.2 SW	509069010	53 $^{\circ}$ .49	-2 $^{\circ}$ .18	2014/4/14 12:40:57	2014/4/15 01:45:12	24.2
3C400.2 SE	509070010	53 $^{\circ}$ .58	-2 $^{\circ}$ .41	2014/4/23 22:36:02	2014/4/24 11:25:13	25.0
3C400.2 NE	509071010	53 $^{\circ}$ .76	-2 $^{\circ}$ .41	2014/4/23 00:41:40	2014/4/23 11:08:11	20.2
EMS 1308	405028010	54 $^{\circ}$ .37	0 $^{\circ}$ .06	2010/4/27 10:28:40	2010/4/27 23:26:20	23.9

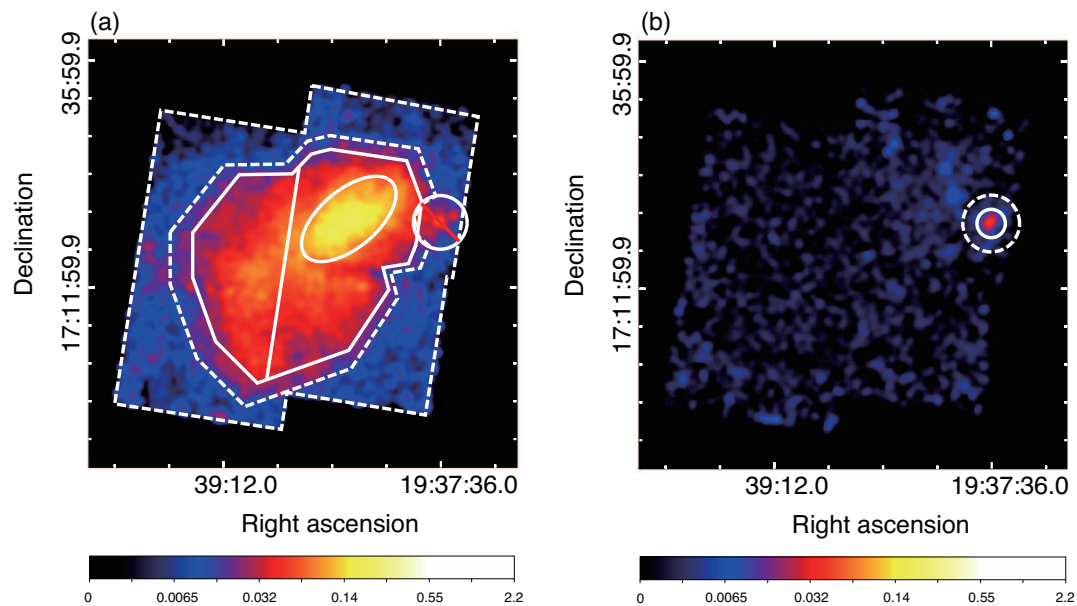


**Fig. 1.** (a) Suzaku XIS image of 3C 400.2 in the 0.5–3.0 keV energy band. The NXB is subtracted, and the vignetting effect is corrected. The images of XIS0, 1, and 3 are all merged. The whole SNR region is enclosed by a solid polygon, and it is divided into two regions by a solid line, the “east” and “west” regions. An ellipse indicates the “bright” region. The “dim” region is the whole SNR region excluding the bright region. The BGD region is surrounded by white dashed lines. A point-like source, which is indicated by a circle, is excluded from the SNR and BGD spectra. (b) Same as (a), but the 3.0–5.0 keV energy-band image. The point-like source spectrum and the background spectrum are extracted from the solid circle and an annular region enclosed by the solid and dashed circles, respectively.

we made other two ARFs for the BGD spectrum: one is for the SNR emission contaminating the BGD region due to the out-skirt of the PSF, and the other is for the background emission observed in the BGD region.

Since 3C 400.2 is located in the inner region of our Galaxy, the background emission is composed of the foreground emission (FE; e.g. the local hot bubble), the Galactic ridge X-ray emission (GRXE), and the cosmic X-ray background (CXB). Referring to Uchiyama et al. (2013), we adopted the following model for the background emission;  $\text{Abs1} \times \text{FE} + \text{Abs2} \times (\text{HP}_{\text{GRXE}} + \text{LP}_{\text{GRXE}} + \text{CM} + \text{Abs2} \times \text{CXB})$ . “Abs1” and “Abs2” mean the interstellar absorptions for the FE and the GRXE, respectively, and the hydrogen column densities  $N_{\text{H}}$

of the individual components are free parameters. “FE” consists of two-temperature CIE plasmas, and we fixed the parameters other than the normalizations to those of Uchiyama et al. (2013). The GRXE components “HP” and “LP” are high- and low-temperature plasmas, respectively. We fixed their parameters other than the normalizations to those of Uchiyama et al. (2013). “CM” comes from the cold matter and is composed of the neutral Fe  $K\alpha$  and  $K\beta$  lines and the power-law emission associated with them. We fixed all the parameters of “CM” (the centroids, the equivalent widths, and the flux ratio of the  $K\alpha$  and  $K\beta$  lines) other than the flux of the Fe  $K\alpha$  line to those of Uchiyama et al. (2013). “CXB” is expressed as a power-law function, whose photon index and flux were fixed to those of

Kushino et al. (2002).

We found that the simultaneous fitting resulted in large uncertainties of the flux ratio of “FE”, “HP”, and “LP” because the fluxes of the components were degenerated. Then we referred to a spectrum of the nearby region (EMS 1308) to constrain the flux ratio of the background components. The nearby-region spectrum was well explained by the background model. The Galactic longitude of the FOV of the nearby region is almost the same as the SNR coordinate, but the Galactic latitude is lower than the SNR’s (see table 1). Since the HP and LP fluxes depend on the Galactic coordinates, we scaled the best-fit fluxes of “HP” and “LP” in the nearby region to that of the central position of 3C 400.2 by the scale heights obtained by Yamauchi et al. (2016).

We can now conduct the simultaneous fitting of the whole SNR and BGD spectra. The X-ray spectra in the high-energy band were dominated by the CXB. This is consistent with the X-ray image in the high-energy band (figure 1b), where no structures other than the point-like source are found. In addition, the ratio of the NXB to the signal increases in the high-energy band. Therefore, the energy band above 5 keV is discarded in the following analysis. We will describe the detail and fitting result in the next section.

### 3.3 Simultaneous fitting of the whole SNR and BGD spectra

In the simultaneous fitting described below, we found that there are residuals in the BGD spectrum at the Ne and Mg K-shell lines of  $\sim 1.0$  keV and  $\sim 1.3$  keV, respectively, regardless of the SNR emission models we tried. These lines are dominated by the “FE” component with the temperature of 0.59 keV. Uchiyama et al. (2013) examined abundances of the GRXE spectrum above 2 keV, and thus Ne and Mg abundances were not constrained. We let the Ne and Mg abundances of the “FE” component free.

We first assumed that the SNR emission comes from a one-temperature IP, and adopted the `phabs×vnei` model in XSPEC. All the parameters of the SNR model other than abundances were set as free parameters. The abundances of Ne, Mg, Si, S, Ar, Ca, Fe, and Ni were free, while the other abundances were fixed to the solar ones. Since the line intensities of Ar, Ca, Fe, and Ni are not strong enough, the abundances of Ar and Ca, and those of Fe and Ni were linked, respectively. The best-fit model could not explain the SNR spectra in the low-energy band, especially around  $\sim 1.3$  keV and  $\sim 1.9$  keV. The reduced  $\chi^2$  was 1.85 (d.o.f.=613), which is not acceptable. Then we adopted a two-temperature IP model; `phabs×(vnei+vnei)`. Assuming that the low- and high-temperature components are of the ISM and ejecta origins, respectively, we allowed the Ne, Mg, Si, S, Ar, Ca, Fe, and Ni abundances of the high-temperature component

**Table 2.** Best-fit parameters of BGD region spectrum.

Component	Parameter	Value
Abs1	$N_{\text{H}}$ ( $10^{22}$ cm $^{-2}$ )	$1.03^{+0.01}_{-0.04}$
FE (CIE)	$kT_{\text{e}}$ (keV)	0.09 (fixed) <sup>  </sup>
	Abundance <sup>*</sup>	0.05 (fixed) <sup>  </sup>
	Norm <sup>†</sup>	$28 \pm 4$
FE (CIE)	$kT_{\text{e}}$ (keV)	0.59 (fixed) <sup>  </sup>
	$Z_{\text{Ne}}$ <sup>*</sup>	$0.25^{+0.07}_{-0.10}$
	$Z_{\text{Mg}}$ <sup>*</sup>	$0.15^{+0.04}_{-0.03}$
	$Z_{\text{Other}}$ <sup>*</sup>	0.05 (fixed) <sup>  </sup>
	Norm <sup>†</sup>	$(5.0 \pm 0.5) \times 10^{-3}$
Abs2	$N_{\text{H}}$ ( $10^{22}$ cm $^{-2}$ )	$2.70^{+0.21}_{-0.18}$
HP (CIE)	$kT_{\text{e}}$ (keV)	6.64 (fixed) <sup>  </sup>
	$Z_{\text{Ar}}$ <sup>*</sup>	1.07 (fixed) <sup>  </sup>
	$Z_{\text{Other}}$ <sup>*</sup>	0.81 (fixed) <sup>  </sup>
	Norm <sup>†</sup>	$1.3 \times 10^{-4}$ (fixed)
LP (CIE)	$kT_{\text{e}}$ (keV)	1.33 (fixed) <sup>  </sup>
	$Z_{\text{Ar}}$ <sup>*</sup>	1.07 (fixed) <sup>  </sup>
	$Z_{\text{Other}}$ <sup>*</sup>	0.81 (fixed) <sup>  </sup>
	Norm <sup>†</sup>	$2.0 \times 10^{-3}$ (fixed)
CM (Fe I K $\alpha$ )	centroid (keV)	6.40 (fixed) <sup>  </sup>
	Norm <sup>‡</sup>	$< 5.2 \times 10^{-8}$
CM (Fe I K $\beta$ )	centroid (keV)	7.06 (fixed) <sup>  </sup>
	Norm <sup>‡</sup>	Norm <sub>6.4</sub> $\times$ 0.125
CM (Power law)	$\Gamma$	2.13 (fixed) <sup>  </sup>
	$EW_{6.4}$ (eV)	547 (fixed) <sup>  </sup>
CXB (Power law)	$\Gamma$	1.4 (fixed) <sup>‡</sup>
	Norm <sup>§</sup>	$8.6 \times 10^{-5}$ (fixed) <sup>‡</sup>

<sup>\*</sup> Relative to the solar values in Anders et al. (1989).

<sup>†</sup> Defined as  $\frac{10^{-14}}{4\pi D_A^2} \int n_e n_H dV$ .  $D_A$  is the angular diameter distance to the source.  $dV$  is the volume element, and  $n_e$  and  $n_H$  are the electron and hydrogen densities, respectively. The unit is cm $^{-5}$ .

<sup>‡</sup> The unit is photons cm $^{-2}$  s $^{-1}$ .

<sup>§</sup> The unit is photons keV $^{-1}$  cm $^{-2}$  s $^{-1}$  at 1 keV.

<sup>||</sup> The values are fixed Uchiyama et al. (2013).

<sup>‡</sup> The values are fixed Kushino et al. (2002).

to be free, while the other abundances, including those of the low-temperature component, were fixed to the solar ones. The reduced  $\chi^2$  of the fitting was 1.69 (d.o.f.=610), which is still unacceptable. We found residuals at  $\sim 0.8$  keV and  $\sim 1.2$  keV. It would be due to the incomplete atomic data for Fe L-shell emission lines in the XSPEC model (e.g., Nakashima et al. 2013). We added two Gaussians to represent these features, which decreased the reduced  $\chi^2$  to 1.15 (d.o.f.=606). The best-fit ionization timescale ( $\tau = n_e t$ ) of the low-temperature component was  $7.3 \times 10^{12} \text{ cm}^{-3} \text{ s}$ . This value indicates that the plasma has already reached to the CIE state. We finally adopted the SNR model of `phabs*(vapec+vnei+gaussian+gaussian)`, where we regard the low-temperature component as the CIE plasma. Figures 2(a) and (b) show the simultaneous fitting results of the BGD and the whole SNR spectra, respectively. The simultaneous fitting revealed that the background emission contributes to 10% of all the X-ray emissions in the whole SNR region, while the SNR emission contaminating in the BGD region accounts for 5.8% of the X-ray emission there. Tables 2 and 3 show the best-fit parameters of the BGD and the whole SNR spectra, respectively.

Broersen et al. (2015) analyzed the Chandra data and explained a 3C 400.2 spectrum with a two-temperature plasma model: an RP originating from the ISM ( $kT_e \sim 0.1$  keV) plus an IP originating from the ejecta ( $kT_e \sim 3$  keV). To examine whether the model is valid, we fitted the whole SNR spectra with the model referred by Broersen et al. (2015), adding the Fe-L lines, `phabs*(vrnei+vrnei+gaussian+gaussian)` in XSPEC. The fitting resulted in positive residuals at  $\sim 0.7$  keV and the He-like Si line, and the model was rejected by the reduced- $\chi^2$  value of 3.92 (d.o.f.=404).

### 3.4 Spectral analysis of the bright and dim regions

The X-ray image of 3C 400.2 (figure 1a) shows a bright emission in the northwestern region surrounded by a relatively dim emission. To investigate the difference in the plasma parameters depending on the brightness, we divided the whole SNR region into two regions, “bright” (the eclipse with the radii of  $3.0'$  and  $6.0'$  in figure 1a) and “dim” (the whole SNR region excluding the eclipse), and extracted spectra from each region.

Similar to the simultaneous fitting of the whole SNR and the BGD spectra, we fitted a source spectrum with the two ARFs; one for the SNR emission model and the other for the background model. We used the background model that was obtained by the simultaneous fitting of the whole SNR and BGD spectra, with all the parameters of the model fixed to the best-fit ones in the simultaneous fitting, except for the normalizations, which were scaled by the sky areas of the source region.

The SNR emission model is the same as the best-fit one in the simultaneous fitting,

`phabs*(vapec+vnei+gaussian+gaussian)` in XSPEC. We allowed the hydrogen column density  $N_H$ , the temperatures  $kT_e$ , the ionization time scale  $\tau$ , the abundances of Ne, Mg, Si, S, Ar, Ca, Fe, and Ni (in `vnei`), and the normalizations to be free. The model explained the spectra of both the regions well. The obtained reduced- $\chi^2$  values of the “bright” and “dim” spectra were 0.94 (d.o.f.=409) and 1.06 (d.o.f.=394), respectively. The spectra are shown in figures 2(c) and (d), and the best-fit parameters are listed in table 3.

### 3.5 Spectral analysis of the east and west regions

The Suzaku data we analyzed was previously studied by Ergin et al. (2017), who divided the SNR region into four regions, NW, SW, SE, and NE, and found an RP in the SE and NE regions. To examine the RP scenario, we extracted spectra from the “east” region (roughly a sum of SE and NE) as well as from the “west” region (roughly a sum of NW and SW). The source regions are shown in figure 1(a). We used the background model that was obtained by the simultaneous fitting of the whole SNR and BGD spectra, and all the parameters were fixed to the best-fit ones in the previous simultaneous fitting, except for the normalizations, which were scaled by the sky areas. We fitted each region’s spectra with the two ARFs; one is for the SNR emission model and the other for the background model.

We adopted the same SNR emission model as was obtained by the fitting of the whole region spectrum, `phabs*(vapec+vnei+gaussian+gaussian)` in XSPEC. The free parameters are the same as in the fitting of the “bright” and “dim” spectra. Our model explained the “east” and “west” spectra well. The reduced- $\chi^2$  values of the “east” and “west” spectra were 1.07 (d.o.f.=406) and 1.12 (d.o.f.=391), respectively. The spectra are shown in figures 2(e) and (f), and the best-fit parameters are listed in table 3. We also fitted the “east” spectrum with the model referred by Ergin et al. (2017), adding the Fe-L lines, `phabs*(vrnei+vrnei+gaussian+gaussian)` in XSPEC. The model was rejected by the reduced- $\chi^2$  value of 3.60 (d.o.f.=419); there were remarkable positive residuals in the Si and S lines.

### 3.6 Spectral analysis of Suzaku J1937.4+1718

We extracted FI and BI spectra from the  $1.5'$  circle around the unidentified source, Suzaku J1937.4+1718, as well as from the annular region around the circle with the radius of  $3.0'$  for the background subtraction (figure 1b).

We fitted the background-subtracted spectra with an absorbed power-law. The spectra show line-like residuals at  $\sim 4.4$  keV. We then fit the spectra with the model consisting of an absorbed power-law plus a gaussian (model A). The line fea-

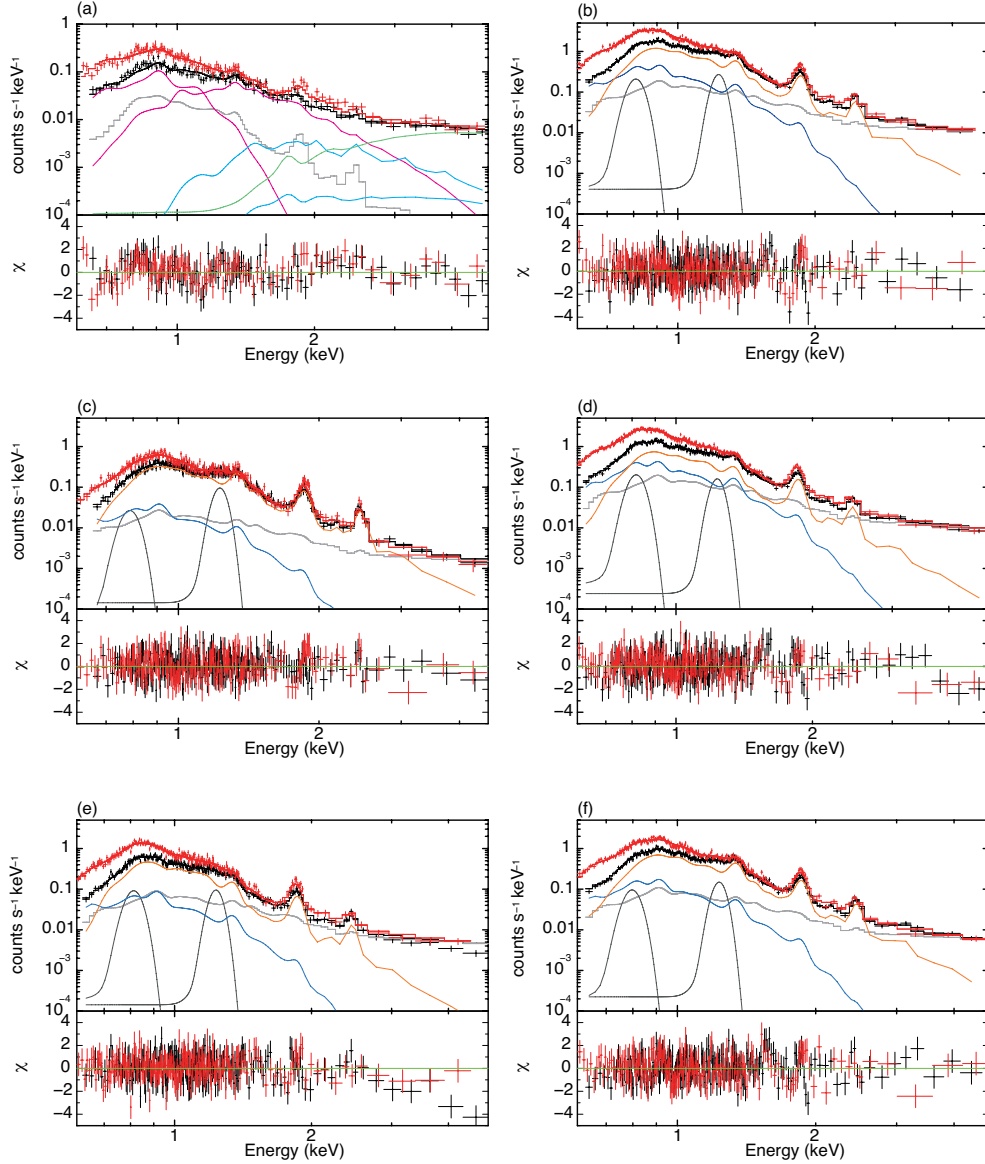


**Fig. 2.** (a) BGD spectra with the best-fit background model. The magenta, cyan, green, and gray lines indicate “FE”, “LP” and “HP”, “CXB”, and the contamination of the SNR 3C 400.2, respectively. (b) Whole SNR spectra with the best-fit model. The blue, orange, black, and gray lines show the low-temperature plasma, the high-temperature plasma, the Fe-L lines, and the background model, respectively. The BGD spectra (a) and whole SNR spectra (b) are simultaneously fitted. (c) “dim” region spectra. The color indication is the same as (b). (d) Same as (c), but for the “bright” region spectra. (e) Same as (c), but for the “east” region. (f) Same as (c), but for the “west” region. The black and red data show the FI and BI spectra, respectively.

ture at  $4.4 \pm 0.1$  keV was detected with the significance level of  $2.8\sigma$  and the line equivalent width (EW) is measured to be  $340_{-270}^{+560}$  eV (table 4). Since there is no striking atomic line at the rest energy around  $\sim 4.4$  keV, the line feature could be due to a red-shifted Fe line; a neutral Fe line at 6.4 keV or He-like Fe line at 6.7 keV in the rest frame. If the former is the case, the redshift is calculated to be  $z = 0.46_{-0.04}^{+0.03}$ . Assuming the latter case, we also fit the spectra with an absorbed CIE plasma model (model B). We obtained the electron temperature  $kT_e$  of  $8.2_{-2.9}^{+8.0}$  keV and the redshift of  $z = 0.55_{-0.04}^{+0.05}$ . The

best-fit parameters of model A and model B are shown in table 4. The spectra are shown in figure 3. The flux of the point-like source in the 0.2–16 keV band is measured to be  $6.7_{-2.1}^{+0.3} \times 10^{-13}$  erg s $^{-1}$  cm $^{-2}$  and  $6.0_{-2.6}^{+0.8} \times 10^{-13}$  erg s $^{-1}$  cm $^{-2}$  for model A and model B, respectively.

**Table 3.** Best-fit parameters of 3C 400.2.

Component	Parameter	Value				
		whole	bright	dim	east	west
Absorption	$N_{\text{H}}^*$	$0.54^{+0.01}_{-0.02}$	$0.54^{+0.02}_{-0.03}$	$0.57^{+0.03}_{-0.02}$	$0.50^{+0.02}_{-0.01}$	$0.52^{+0.01}_{-0.02}$
CIE	$kT_{\text{e}}$ (keV)	$0.23^{+0.01}_{-0.02}$	$0.20 \pm 0.03$	$0.24 \pm 0.01$	$0.20^{+0.03}_{-0.03}$	$0.22^{+0.01}_{-0.03}$
	Abundance <sup>†</sup>	1.0 (fixed)	1.0 (fixed)	1.0 (fixed)	1.0 (fixed)	1.0 (fixed)
	Norm <sup>  </sup>	$14 \pm 2$	$2.8^{+4.1}_{-1.7}$	$13 \pm 2$	$5.5^{+2.4}_{-1.3}$	$7.3^{+1.5}_{-0.6}$
IP	$kT_{\text{e}}$ (keV)	$0.75 \pm 0.01$	$0.81^{+0.01}_{-0.03}$	$0.75 \pm 0.02$	$0.69^{+0.02}_{-0.01}$	$0.80^{+0.03}_{-0.02}$
	$Z_{\text{Ne}}^{\dagger}$	$1.5 \pm 0.1$	$1.6^{+0.8}_{-0.6}$	$2.5 \pm 0.5$	$3.7^{+1.0}_{-0.8}$	$1.2 \pm 0.2$
	$Z_{\text{Mg}}^{\dagger}$	$2.3^{+0.7}_{-0.4}$	$4.3^{+2.4}_{-0.9}$	$3.2 \pm 0.2$	$4.6 \pm 0.5$	$2.1^{+0.1}_{-0.3}$
	$Z_{\text{Si}}^{\dagger}$	$2.7 \pm 0.3$	$3.7^{+1.6}_{-0.9}$	$4.6^{+2.2}_{-0.3}$	$6.9 \pm 0.7$	$1.9^{+0.2}_{-0.1}$
	$Z_{\text{S}}^{\dagger}$	$3.8^{+1.3}_{-1.1}$	$6.7^{+2.2}_{-2.1}$	$5.7^{+1.0}_{-0.9}$	$9.0^{+2.5}_{-2.4}$	$3.0 \pm 0.4$
	$Z_{\text{Ar,Ca}}^{\dagger}$	$<5.7$	$<2.3$	$<10$	$<6.0$	$<4.5$
	$Z_{\text{Fe,Ni}}^{\dagger}$	$3.7^{+0.2}_{-0.8}$	$4.6^{+2.7}_{-1.1}$	$7.0^{+0.6}_{-0.9}$	$12 \pm 1$	$2.3^{+0.3}_{-0.2}$
	$Z_{\text{other}}^{\dagger}$	1.0 (fixed)	1.0 (fixed)	1.0 (fixed)	1.0 (fixed)	1.0 (fixed)
	$\tau^{\ddagger}$	$1.9^{+0.2}_{-0.3}$	$1.6^{+0.3}_{-0.4}$	$1.5 \pm 0.3$	$1.4^{+0.4}_{-0.2}$	$1.4^{+0.3}_{-0.2}$
	Norm <sup>  </sup>	$1.6 \pm 0.2$	$0.48^{+0.13}_{-0.09}$	$0.69^{+0.04}_{-0.12}$	$0.3 \pm 0.1$	$1.7 \pm 0.1$
$\chi^2/\text{d.o.f}$		$691.21/608=1.14$	$384.59/409=0.94$	$417.93/394=1.06$	$435.31/406=1.07$	$437.98/391=1.12$

\* The unit is  $10^{22} \text{ cm}^{-2}$ .

† Relative to the solar values in Anders et al. (1989).

‡ Ionization timescale. The unit is  $10^{11} \text{ cm}^{-3} \text{ s}$ .

|| Defined as  $\frac{10^{-14}}{4\pi D_A^2} \int n_e n_H dV$ .  $D_A$  is the angular diameter distance to the source.  $dV$  is the volume element, and  $n_e$  and  $n_H$  are the electron and hydrogen densities, respectively. The unit is  $10^{-3} \text{ cm}^{-5}$ .

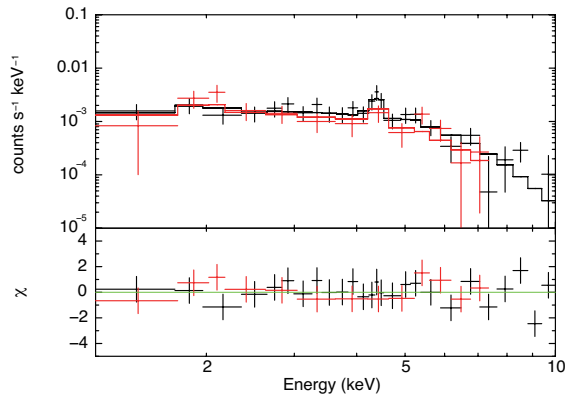


**Fig. 3.** Background-subtracted spectra Suzaku J1937.4–1718 fitted with the absorbed CIE model (model B). The black and red data represent the FI and BI spectra, respectively.

## 4 Discussion

### 4.1 SNR plasma of 3C 400.2

We adapted the whole SNR spectra with the two-temperature model: the low-temperature ( $\sim 0.2$  keV) CIE plasma plus the high-temperature ( $\sim 0.8$  keV) IP. On the assumption that the former would be of the ISM heated by a blast wave while the latter would be of the ejecta origin, we fixed the abundances of the low-temperature plasma to 1 solar whereas those of Ne, Mg, Si, S, Ar, Ca, Fe, and Ni of the high-temperature plasma were

free parameters. The model explained the whole SNR spectra well. Although the abundances of Ar and Ca were only constrained by the upper limit, those of the other elements were obtained to be higher than 1 solar.

Assuming that the distance of the SNR is  $D = 2.8$  kpc (Giacani et al. 1998) and the plasma of the whole SNR region is shaped like a sphere with a 12-arcmin radius, the X-ray emitting volume is estimated to be  $V = 1.1 \times 10^{59} f \text{ cm}^3$ . Here,  $f$  is a filling factor. The best-fit normalization of the ejecta component is defined as  $\frac{10^{-14}}{4\pi D^2} \int n_e n_H dV \sim \frac{10^{-14}}{4\pi D^2} n_e n_H V$ , where  $n_e$  and  $n_H$  are the electron and Hydrogen densities, respectively, and is obtained to be  $1.6 \times 10^{-3} \text{ cm}^{-5}$  as shown in table 3. On the assumption of the density ratio  $n_e/n_H = 1.2$ , we estimated the averaged electron density of the ejecta to be  $n_e \sim 0.04 f^{-1/2} \text{ cm}^{-3}$ , and then obtained the ionization timescale of  $t = \tau/n_e \sim 1.5 \times 10^5 f^{1/2} \text{ yr}$  for the whole region. This is compatible with the SNR age estimated by the previous studies ( $10^4$ – $10^5$  yr; Long et al. 1991; Rosado 1983). The low density of the ejecta preserves the plasma in the ionizing state despite the old age of 3C 400.2. We calculated the total ejecta mass by  $M_{\text{ejecta}} \sim \sum_i \eta_i n_H Z_i m_i V$ , where  $\eta_i$ ,  $Z_i$ ,  $m_i$  are the abundance ratio to Hydrogen in the solar abundance (Anders et al. 1989), the ejecta abundance relative to the solar ones, and the mass of each element ( $i = \text{He, C, N, O, Ne, Mg, Si, S, Ar, Ca, Fe, and Ni}$ ). The obtained ejecta mass is  $M_{\text{ejecta}} \sim 4.5 M_{\odot} f^{1/2}$ , which indicates the core-collapse (CC) supernova origin.

**Table 4.** Best-fit parameters of Suzaku J1937.4+1718.

Model	Parameter	Value
model A		
Absorption	$N_{\text{H}}$ ( $10^{22}$ cm $^{-2}$ )	$2.8_{-1.0}^{+1.4}$
Power law	$\Gamma$	$2.2_{-0.5}^{+0.6}$
	Norm*	$3.4_{-1.9}^{+5.2}$
Gaussian	centroid (keV)	$4.4 \pm 0.1$
	width (eV)	0 (fixed)
	Norm $^{\dagger}$	$4.3 \pm 2.5$
	EW $_{\text{gauss}}$ (eV) $^{\ddagger}$	$340_{-270}^{+560}$
$\chi^2/\text{d.o.f.}$		47.23/29=1.63
model B		
Absorption	$N_{\text{H}}$ ( $10^{22}$ cm $^{-2}$ )	$2.1_{-0.7}^{+1.0}$
CIE	$kT_{\text{e}}$ (keV)	$8.2_{-2.9}^{+8.0}$
	Abundance $^{\parallel}$	$0.75_{-0.47}^{+1.86}$
	redshift	$0.55_{-0.04}^{+0.05}$
	Norm $^{\#}$	$1.1_{-0.5}^{+0.7}$
$\chi^2/\text{d.o.f.}$		42.34/29=1.46

\* The unit is  $10^{-4}$  photons keV $^{-1}$  cm $^{-2}$  s $^{-1}$  at 1 keV.

$^{\dagger}$  The unit is  $10^{-6}$  photons cm $^{-2}$  s $^{-1}$ .

$^{\ddagger}$  Equivalent width.

$^{\parallel}$  Relative to the solar values in Anders et al. (1989).

$^{\#}$  Defined as  $\frac{10^{-14}}{4\pi[D(1+z)]^2} \int n_{\text{e}} n_{\text{H}} dV$ .  $D$  is the distance to the source.  $dV$  is the volume element, and  $n_{\text{e}}$  and  $n_{\text{H}}$  are the electron and hydrogen densities, respectively. The unit is  $10^{-3}$  cm $^{-5}$ .

We estimated the progenitor of 3C 400.2 using the abundance ratio of the ejecta components. Katsuda et al. (2018) investigated a progenitor mass distribution of core-collapse SNRs in our Galaxy and Large and Small Magellanic Clouds and elucidated that the Fe/Si ratio is sensitive to the progenitor's zero-age main-sequence mass  $M_{\text{ZAMS}}$ . According to their classification, the Fe/Si ratio observed in 3C 400.2,  $1.4_{-0.3}^{+0.2}$ , indicates the progenitor with  $M_{\text{ZAMS}} < 15M_{\odot}$ , which is the lowest mass group among core-collapse SNRs. In fact, the Fe/Si ratio of the SNR is notably higher compared to other core-collapse SNRs, suggesting significant production of  $^{56}\text{Ni}$ . One possible scenario for the progenitor of 3C 400.2 is a hydrogen-poor stripped-envelope supernova, which can produce at least three times as much  $^{56}\text{Ni}$  as other classes of core-collapse supernovae can (Anderson 2019; Afsariardchi et al. 2021).

We analyzed the “bright” and “dim” spectra to see the difference in the plasma parameters depending on the brightness. The temperatures of the ISM components as well as the abundances and the ionization time scales of the ejecta components are consistent between the two regions within the 90% confidence level. On the other hand, one of the differences in the

parameters is the electron temperature of the ejecta component, which is higher in the “bright” region ( $0.81_{-0.03}^{+0.01}$  keV) than in the “dim” region ( $0.75 \pm 0.02$  keV). Another difference is the ISM density. Assuming that the volumes of the bright region as an ellipsoid with radii of  $3.0'$ ,  $3.0'$ , and  $6.0'$ , we estimated the electron density of the ISM component in the “bright” region to be  $\sim 0.29f^{-1/2}$  cm $^{-3}$ , which is about 2.4 times higher than that of the dim region ( $\sim 0.12f^{-1/2}$  cm $^{-3}$ ). The previous study (Ergin et al. 2017) found an indication of the interaction between the SNR shell and the H I cloud located in the northwest of the SNR. The higher density of the ISM component in the “bright” region would come from the H I gas. In summary, a plausible scenario is that 3C 400.2 is a remnant of a core-collapse supernova (possibly a hydrogen-poor stripped-envelope supernova), which exploded in the H I gas cavity near the “bright” region.

## 4.2 Comparison with the previous studies

Our analysis revealed that the 3C 400.2 spectra are explained by a combination of the CIE plasma and the IP, in contrast to the previous studies which explained the SNR spectra with the RP model. We discuss possible causes of the discrepancy between the previous studies and this study.

Broersen et al. (2015) reported that radiative recombination continua (RRCs) are seen in the 0.5–1.7 keV band in the Chandra spectrum. In this study, however, the RRCs were not found in the whole SNR spectra. A difference in the analysis between Broersen et al. (2015) and this study is the methods of the background estimation; Broersen et al. (2015) produced the background spectra by using the standard ACIS-I background files, whereas we conducted the simultaneous fitting. Broersen et al. (2015) found the SNR emission even above 3 keV in the background-subtracted spectra, but we found that the spectra above 3 keV is dominated by the background emission as shown in figure 2(b). We consider that the Chandra study would have underestimated the background emission. In fact, Broersen et al. (2015) obtained a much higher temperature of  $kT_{\text{e}} \sim 3$  keV than those obtained by Ergin et al. (2017) and this study. The higher the plasma temperature, the more insufficient the continuum emission in the low-energy band. We infer that the low-temperature RP of the Broersen et al. (2015) model is required to complement the insufficient continuum with the RRCs.

Ergin et al. (2017) reported that the SNR emission in the NE and SE regions is explained by the RP of the ejecta origin as well as the CIE plasma of the ISM origin. On the other hand, we found that the SNR emission in the east region can be explained by the IP of the ejecta origin and the CIE plasma of the ISM origin, despite analyzing the same Suzaku data as the authors did. Ergin et al. (2017) found that the spectra of the NW and SW regions are expressed by the CIE plasma and IP, which is consistent with this study. The difference between



Ergin et al. (2017) and this study in the east region is also attributable to the difference in the background estimation. Ergin et al. (2017) estimated the background spectra by extracting the data from nearby regions of the same FOVs as the SNR. The nearby-region spectra contain contamination from the 3C 400.2 emission with the strong line emissions as demonstrated in this study. Therefore, subtracting the nearby-region spectra from the source ones leads to an overestimation of the background emission, especially in the emission lines. The RP model was needed in the Ergin et al. (2017) study because it would explain the weaker line intensities than those expected from the electron temperature in the IP or CIE plasma model. Meanwhile, since the NW and SW spectra have larger normalizations than the NE and SE ones, the NW and SW spectra were less affected by the background subtraction, and thus they were explained by the same model as this study.

### 4.3 Origin of Suzaku J1937.4+1718

We discovered the unidentified source Suzaku J1937.4+1718. The hydrogen column density of the source ( $N_{\text{H}} = 2.8_{-1.0}^{+1.4} \times 10^{22} \text{ cm}^{-2}$  in model A) is five times as large as that of 3C 400.2 ( $N_{\text{H}} = 0.54_{-0.02}^{+0.01} \times 10^{22} \text{ cm}^{-2}$ ), which implies the extragalactic origin. Moreover, we detected the line structure at  $E \sim 4.4 \text{ keV}$  with the  $2.8\sigma$  significance level in the X-ray spectra. Since there are no striking atomic lines at this energy in the rest frame, the line would be due to a redshifted Fe line, and the source is considered to be an active galactic nucleus (AGN) or a cluster of galaxies (CG).

Assuming that the source is an AGN and fitting the spectra with the model consisting of an absorbed powerlaw and a gaussian representing a redshifted Fe I  $K\alpha$  line, we obtained the redshift and the X-ray luminosity (2–8 keV) to be  $0.46_{-0.04}^{+0.03}$  and  $2.6 \times 10^{44} h_{70}^{-2} \text{ erg s}^{-1}$ , respectively. The luminosity lies in typical values of AGNs (e.g. Silverman et al. 2008). The measured equivalent width of the Fe line ( $340_{-270}^{+560} \text{ eV}$ ) is marginally larger than those of typical AGNs (50–200 eV; Ricci et al. 2014) although the error ranges are large.

If the source is a CG, the 4.4-keV line would come from a Fe XXV  $K\alpha$  line. The spectral analysis obtained the electron temperature of  $kT_e = 8.2_{-2.9}^{+8.0} \text{ keV}$ . Using  $H_0 = 70 h_{70} \text{ km s}^{-1} \text{ Mpc}^{-1}$ ,  $\Omega_{\text{M}} = 0.3$ ,  $\Omega_{\Lambda} = 0.7$  and the measured redshift of  $z = 0.55$ , the distance and the bolometric X-ray luminosity were estimated to be  $2700 h_{70}^{-1} \text{ Mpc}$  and  $5.3 \times 10^{44} h_{70}^{-2} \text{ erg s}^{-1}$ , respectively. The electron temperature and the bolometric luminosity are within the dispersion of the  $L_{\text{X}}-kT$  plot reported by Fukazawa et al. (2004). The Fe abundance of the source ( $Z = 0.75_{-0.47}^{+1.86}$ ) is consistent with that of CGs with the Fe abundance of 0.5 solar (Fukazawa et al. 2000; Matsushita 2011). The CG origin seems to be somewhat more likely than the AGN origin.

Since CGs and AGNs are extended and point sources, respectively, one of the ways to distinguish the two origins is to investigate the spatial extent of the source. We note that, however, even if Suzaku J1937.4+1718 is a CG, its extent can be indistinguishable from a point source due to the XRT's spatial resolution; assuming a typical virial radius of CGs of 1 Mpc (e.g. Walker et al. 2012), the expected apparent extent of the source is  $1/3$ , which is smaller than the spatial resolution (a half-power diameter) of the XRT of  $1/9$  (Serlemitsos et al. 2007).

## 5 Conclusion

Analyzing the Suzaku data, we diagnosed plasma states of the SNR 3C 400.2. To carefully estimate the background emission, we conducted the simultaneous fitting of the spectra extracted from the whole SNR and BGD regions. In contrast to the previous studies, which analyzed the Chandra and Suzaku data and explained the SNR spectra with the RP models, we reproduced the SNR emission by the model consisting of the low-temperature CIE plasma of the ISM origin and the high-temperature IP of the ejecta origin. The discrepancy between the previous studies and this study is considered to be due to the difference of the background estimation methods.

We also discovered the unidentified point-like source named Suzaku J1937.4+1718 near 3C 400.2. The higher hydrogen column density than that of the SNR and the detection of the 4.4-keV line emission with the  $2.8\sigma$  significance level indicate that Suzaku J1937.4+1718 would be an extragalactic source, either an AGN or a CG. A future study with a higher spatial resolution may distinguish its origin.

## Acknowledgments

We are grateful to Satoru Katsuda for providing his valuable comments. This research is supported by MEXT KAKENHI No. JP20K14491, JP20KK0071, 23H00151 (KKN) and JP21K03615 (MN). KKN is also supported by the Yamada Science Foundation and the Mitsubishi Foundation.

## References

- Afsariardchi, N., Drout, M. R., Khatami, D. K., Matzner, C. D., Moon, D. -S., Ni, Y. Q. 2021, *ApJ*, 918, 89
- Ambrocio-Cruz, P., Rosado, M., & de la Fuente, E. 2006, *RMxAA*, 42, 241
- Anders, E., & Grevesse, N. 1989, *Geochim. Cosmochim. Acta*, 53, 197
- Anderson, J. P. 2019, *A&A*, 628, 7
- Broersen, S. & Vink, J. 2015, *MNRAS*, 446, 3885
- Dubner, G. M., Giacani, E. B., Goss, W. M., & Winkler, P. F. 1994, *ApJ*, 108, 207
- Ergin, T., Sezer, A., Sano, H., Yamazaki, R., & Fukui, Y. 2017, *ApJ*, 842, 22

- Fukazawa, Y., Makishima, K., Tamura, T., Nakazawa, K., Ezawa, H., Ikebe, Y., Kiuchi, K., & Ohashi, T. 2000, MNRAS, 313, 21
- Fukazawa, Y., Makishima, K., & Ohashi, T. 2004, PASJ, 56, 965
- Giacani, E. B., Dubner, G., Cappa, C., & Testori, J. 1998, A&AS, 133, 61
- Ishisaki, Y., et al. 2007, PASJ, 59, S113
- Katsuda, S., Takiwaki, T., Tominaga, N., Moriya, T. J., & Nakamura, K. 2018, ApJ, 863, 127
- Konami, S., Matsushita, K., Gandhi, P., & Tamagawa, T. 2012, PASJ, 64, 117
- Koyama, K., et al. 2007, PASJ, 59, S23
- Kushino, A., Ishisaki, Y., Morita, U., Yamasaki, N. Y., Ishida, M., Ohashi, T., & Ueda, Y. 2002, PASJ, 54, 327
- Long, K. S., Blair, W. P., White, R. L., & Matsui, Y. 1991, ApJ, 373, 567
- Matsushita, K. 2011, A&A, 527, A134
- Mitsuda, K., et al. 2007, PASJ, 59, S1
- Nakashima, S., Nobukawa, M., Uchida, H., Tanaka, T., Tsuru, T. G., Koyama, K., Murakami, H., & Uchiyama, H. 2013, ApJ, 773, 20
- Ono, A., Uchiyama, H., Yamauchi, S., Nobukawa, M., Nobukawa, K. K., & Koyama, K. 2019, PASJ, 71, 52
- Rho, J. & Petre, R. 1998, ApJ, 503, L167
- Ricci, C., Ueda, Y., Ichikawa, Y., Paltani, S., Boissay, R., Gandhi, P., Stalevski, M., & Awaki, H. 2014, A&A, 567, 142
- Rosado, M. 1983, Rev. Mex. Astron. Astrofis., 8, 59
- Saken, J. M., Long, K. S., Blair, W. P., & Winkler, P. F. 1995, ApJ, 443, 231
- Serlemitsos, P. J., et al. 2007, PASJ, 59, S9
- Silverman, J. D., et al. 2008, ApJ, 679, 118
- Tawa, N., et al., 2008, PASJ, 60, S11
- Uchiyama, Y., Maeda, Y., Ebara, M., Fujimoto, R., & Ishisaki, Y. 2008, PASJ, 60, S35
- Uchiyama, H., Nobukawa, M., Tsuru, T. G., & Koyama, K. 2013, PASJ, 65, 19
- Walker, S., Fabian, A., Sanders, J., George, M., & Tawara, Y. 2012, AIPC, 1427, 338
- Winkler, P. F., Olinger, T. M., Ratcliff, S. J., & Westerbeke, S. A. 1993, ApJ, 405, 608
- Yamauchi, S., Nobukawa, K. K., Nobukawa, M., Uchiyama, H., & Koyama, K. 2016, PASJ, 68, 59
- Yamauchi, S., & Panutti, T. G. 2023, PASJ, 75, 1273
- Yoshita, K., Tsunemi, H., Miyata, E., & Mori, K. 2001, PASJ, 53, 93